JGR Solid Earth

RESEARCH ARTICLE
10.1029/2021JB023289

3-D Crustal Azimuthal Anisotropy Reveals Multi-Stage Deformation Processes of the Sichuan Basin and Its Adjacent Area, SW China

Zhiqi Zhang[1], Huajian Yao[1,2,3], Weitao Wang[4], and Chuangming Liu[5]

[1]Laboratory of Seismology and Physics of Earth's Interior, School of Earth and Space Sciences, University of Science and Technology of China, Hefei, China, [2]Mengcheng National Geophysical Observatory, University of Science and Technology of China, Hefei, China, [3]CAS Center for Excellence in Comparative Planetology, University of Science and Technology of China, Hefei, China, [4]Institute of Geophysics, China Earthquake Administration, Beijing, China, [5]Department of Physics, University of Colorado Boulder, Boulder, CO, USA

Abstract The collision of the South China Block and the North China Block and the eastward extrusion of the Tibetan Plateau materials have caused complicated tectonic deformation and strong seismicity around the Sichuan Basin (SCB). In order to reveal regional stress distribution and deformation mechanisms, we invert for a 3-D high-resolution shear wave velocity and azimuthal anisotropy model from ambient noise tomography with data from 483 broadband seismographs deployed around the SCB. Our results reveal strong lateral contrasts of azimuthal anisotropy in the crust. The western Sichuan depression shows weak deformation. The central Sichuan uplift, used to be a stable microcontinent, shows relatively strong and coherent fossil anisotropy. In contrast, the eastern Sichuan folds shows strong anisotropy, indicating intense regional deformation. The fast axis direction is bifurcated when reaching the Longmenshan fault, which indicates the obstruction of the SCB to the crustal low velocity materials beneath the Songpan-Ganzi Block. In the east, the rigid SCB and strike-slip faults may transform the compressive stress to shear deformation in adjacent areas and cause a ring-shaped anisotropy pattern below 15 km depth. Furthermore, anisotropy patterns display strong contrast at shallow depths in the Weiyuan and Changning regions, which may facilitate the accumulation of strain and more likely induce earthquakes during the shale gas exploration stage. Our new model provides important constraints for understanding the multi-stage deformation processes in and around the SCB.

Plain Language Summary The rigid Sichuan Basin in SW China has experienced complicated tectonic deformation and faced seismic hazards in its adjacent areas. Therefore, we construct a 3-D high-resolution velocity model in the crust and uppermost mantle to reveal regional structural anomalies and deformation mechanisms in and around the Sichuan Basin. Our model shows weak deformation in western Sichuan Basin, while the central Sichuan Basin shows strong and coherent fossil deformation, indicating its nature as a stable microcontinent. In contrast, the eastern Sichuan Basin shows strong deformation. In particular, the Weiyuan and Changning area in the southeastern Sichuan Basin displays strong contrast in regional deformation patterns, which more likely induce earthquakes. The obstruction of the rigid Sichuan Basin to the weak crustal materials from the Tibetan Plateau causes sharp changes of deformation patterns around the Longmenshan fault zone, the western margin of the Sichuan Basin. Our model provides important information to understand the multi-stage deformation processes and seismic hazards of the Sichuan Basin and its adjacent area.

Key Points:

- Ambient noise tomography reveals three different azimuthal anisotropy patterns and multi-stage deformation processes of the Sichuan Basin
- The eastern margin of the Sichuan Basin shows a ring-shaped azimuthal anisotropy pattern due to compression and shear deformation
- The bifurcated fast axis near the Longmenshan fault indicates the obstruction of the Sichuan Basin to the crustal low velocity materials

Supporting Information:

Supporting Information may be found in the online version of this article.

Correspondence to:

H. Yao,
hjyao@ustc.edu.cn

Citation:

Zhang, Z., Yao, H., Wang, W., & Liu, C. (2022). 3-D crustal azimuthal anisotropy reveals multi-stage deformation processes of the Sichuan Basin and its adjacent area, SW China. *Journal of Geophysical Research: Solid Earth*, *127*, e2021JB023289. https://doi.org/10.1029/2021JB023289

Received 25 SEP 2021
Accepted 12 DEC 2021

Author Contributions:

Conceptualization: Zhiqi Zhang, Huajian Yao
Data curation: Weitao Wang
Funding acquisition: Huajian Yao
Methodology: Huajian Yao, Chuangming Liu
Project Administration: Huajian Yao
Resources: Weitao Wang
Software: Chuangming Liu
Supervision: Huajian Yao
Validation: Zhiqi Zhang, Huajian Yao
Writing – original draft: Zhiqi Zhang
Writing – review & editing: Huajian Yao, Weitao Wang, Chuangming Liu

1. Introduction

The Sichuan Basin (SCB), located in the northwest corner of the South China Block, is a typical cratonic sedimentary basin (He et al., 2011; Kang, 2014). The collision of the South China Block and the North China Block in the late-Indosinia and the expansion of the Xuefeng intracontinental tectonic system in the Cretaceous have formed the trumpet-like opposite protruding arcuate structure in the northeastern SCB (Zhang et al., 2013). In the west, the southeastward movement of the Songpan-Ganzi Block (SPGZ) due to the collision of the Indian and Eurasian plates in the Cenozoic has been obstructed by the rigid SCB and hence formed the steep Longmenshan fault (LMSF) with elevation more than 3,000 m (He et al., 2011; Wei et al., 2008). In the Pre-Sinian crystal

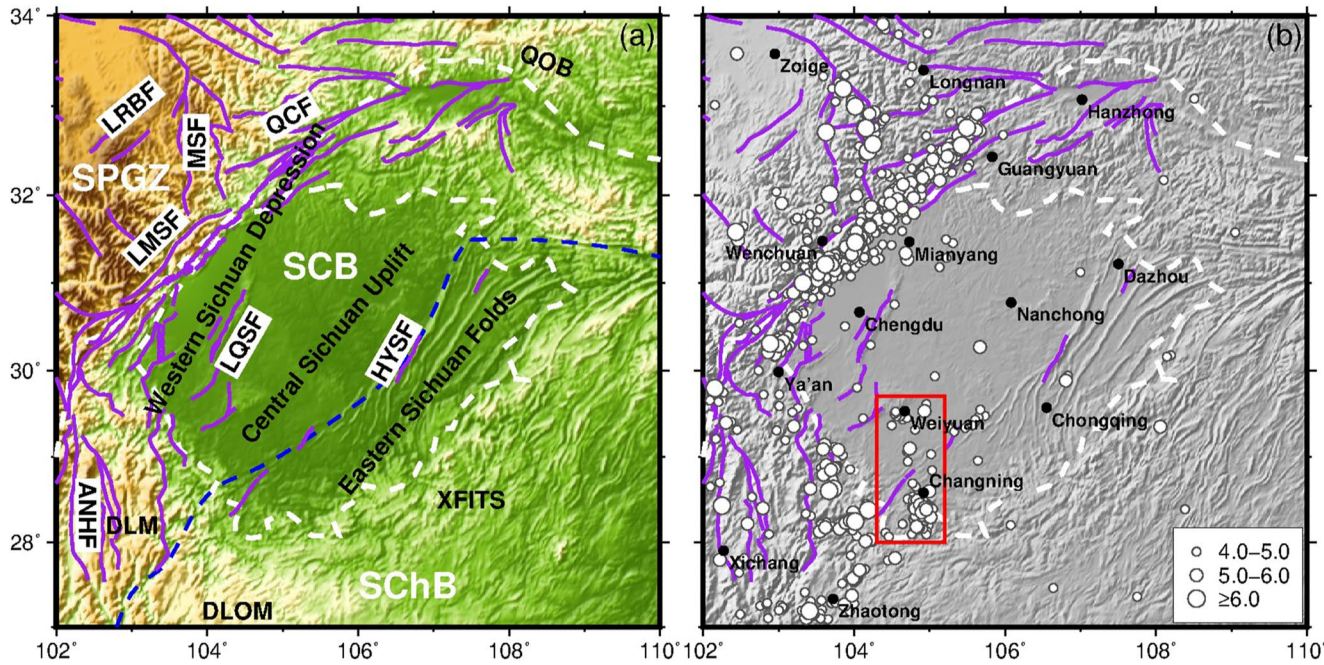

Figure 1. The main geological structures and seismicity in the Sichuan Basin and its surrounding areas. (a) Topography and geological structures. Purple lines represent the major faults in this region (LRBF, the Longriba fault; MSF, the Minshan fault; QCF, the Qingchuan fault; LMSF, the Longmenshan fault; LQSF, the Longquanshan fault; HYSF, the Huayingshan fault; ANHF, the Anninghe fault). Dashed white lines depict the major geological blocks (SPGZ, the Songpan-Ganzi Block; SCB, the Sichuan Basin; SChB, the South China Block). Dashed blue lines represent the Xuefeng intracontinental tectonic system (XFITS) (modified from Zhang et al., 2013). DLM, the Daliang mountain; DLOM, the Dalou mountain; QOB, the Qinling Orogenic Belt. (b) Seismicity in and around the Sichuan Basin. White circles represent earthquakes with $M_w \geq 4.0$ since 1900 (collected from USGS, https://earthquake.usgs.gov), black dots mark the major cities in this region. The red box marks two recent earthquake swarms in Weiyuan and Changning regions, respectively.

basement, the SCB has experienced widespread marine and continental sedimentary deposits. The deposition thickness can reach 6–12 km in the SCB (He et al., 2011; Wang, Hubbard, et al., 2016).

Taking the Longquanshan and Huayingshan faults as the boundaries, the SCB can be divided into three parts. They are the western Sichuan depression, central Sichuan uplift, and eastern Sichuan folds (Figure 1a, He et al., 2011; Xie & Zhang, 1982). The western Sichuan depression is foreland subsidence due to the thrust of the LMSF in the Cenozoic (He et al., 2011; Zhang et al., 2013), and the eastern Sichuan folds is mainly under the extrusion of the Xuefeng intracontinental tectonic system in the Cretaceous and widely develops thin-skinned, Jura-type folds and faults (Wang et al., 2014). Compared with these two parts, however, the central Sichuan uplift possesses fewer folds and faults (Burchfiel et al., 1995). According to the evidence from the positive magnetic anomaly, long-term basement uplift, and absence of many strata, the central Sichuan uplift is thought to have once been a microcontinent, which may be formed in the Proterozoic (He et al., 2011; Xie & Zhang, 1982).

The western margin of the SCB (i.e., the Longmenshan and Anninghe faults) is located in the central part of the North-South seismic belt (He et al., 2019; Wang et al., 2015), which nucleates a lot of earthquakes, including the 2008 M_W 7.9 Wenchuan earthquake, the 2013 M_W 6.6 Lushan earthquake and the 2017 M_W 6.5 Jiuzhaigou earthquake in the past decade. In contrast, there is lack of seismicity inside the SCB, since it is a rigid cratonic basement (Figure 1b).

Sedimentary basins are the main gas reservoirs in the world (Kang, 2014). The SCB was the first natural-gas-producing area in China and now there are about 20 commercial hydrocarbon fields that have been discovered, including the oldest gas field of China in Weiyuan city (Wei et al., 2008). In recent years, many shale gas wells have been drilled in the southeastern SCB, especially in the Weiyuan and Changning regions. Unfortunately, growing seismicity accompanies increasing injection activity (He et al., 2019; Lei et al., 2019), and two swarms of earthquakes formed in Weiyuan and Changning regions with the maximum magnitude up to M_W 5.8 (red box in Figure 1b). However, geoscientists still argue about whether the earthquake swarms are the injection-induced seismicity (Ellsworth, 2013; He et al., 2019; Lei et al., 2019; Wang et al., 2020).

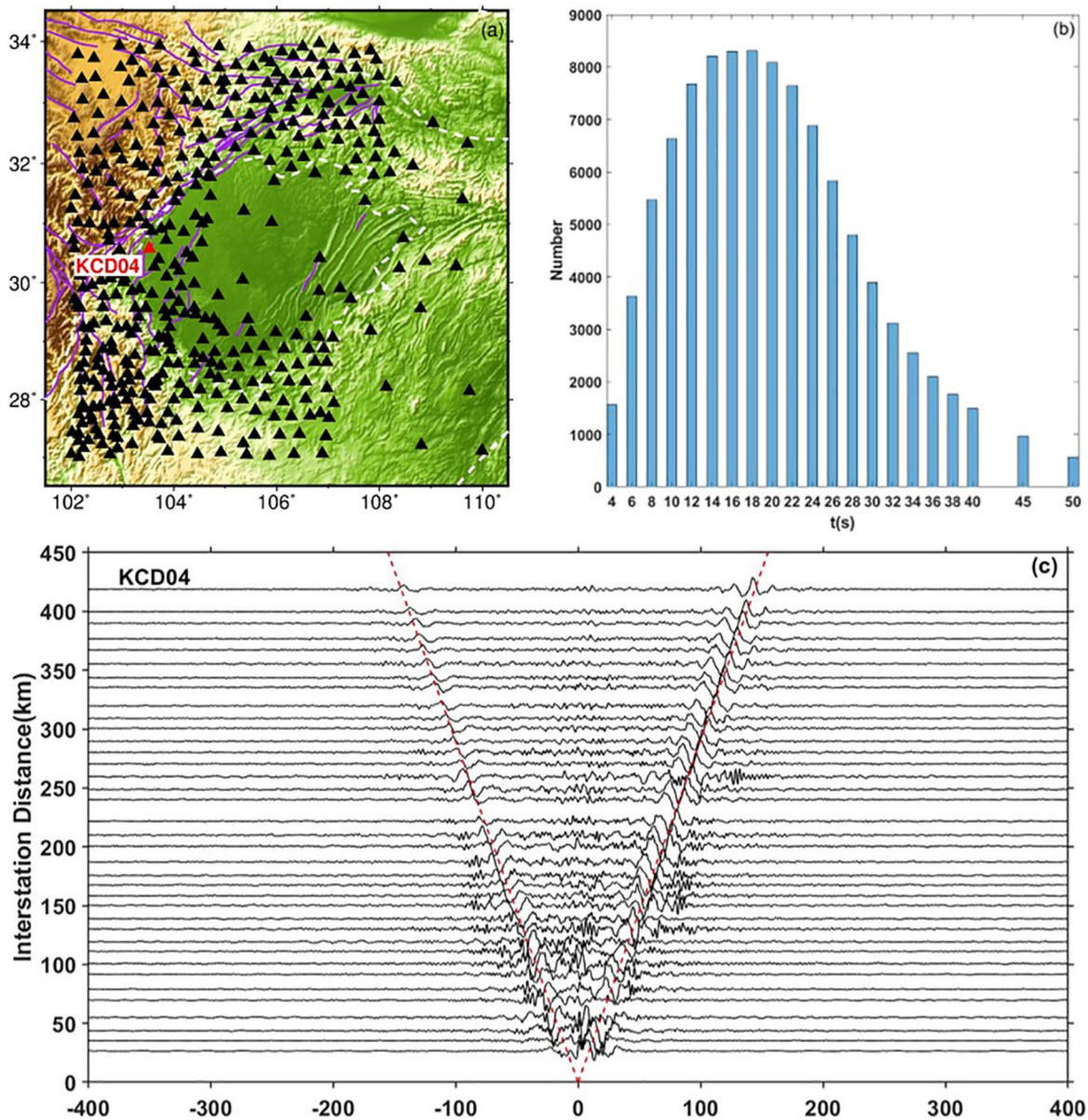

Figure 2. The distribution of stations in the study area (a), the interstation path numbers for different periods (b), and the recovered Rayleigh waves in the period band of 3–50 s from ambient noise cross-correlation between station KCD04 and all other stations with a 10 km distance interval (c). In (a), black triangles mark the stations, purple lines show the faults, and white lines delineate the block boundaries (see Figure 1a in detail). In (c), the location of KCD04 is marked as a red triangle in (a). Dashed red lines represent a group velocity of 2.9 km/s.

The SCB has experienced multistage tectonic evolution and now is under a complex stress background. Increasing seismicity in the western margin of the SCB and the tectonically stable southeastern SCB has caused enormous damages and casualties. A high-resolution tomography model in the crust is particularly needed for understanding the tectonic processes and earthquake hazards of the SCB and its surrounding area. However, due to the lack of seismicity and seismic stations in the SCB (Figures 1b and 2a), there are few high-resolution seismic tomography results in the SCB until now, especially the 3-D anisotropic model that can reveal the deformation features directly.

In this paper, we used ambient noise data from 483 stations in and around the SCB, calculated ambient noise cross-correlation functions, and extracted Rayleigh wave phase velocity dispersion curves in the period range of 3–50 s. We used the direct surface wave inversion method (Liu et al., 2019) to invert for the fine 3-D shear

wave velocity and azimuthal anisotropy structure of the crust and uppermost mantle in the SCB. Then we discuss the azimuthal anisotropy patterns in and around the SCB and its corresponding tectonic stress distribution and deformation mechanisms.

2. Data and Methods

2.1. Data

This study utilized continuous seismic waveforms from 483 broadband stations, including 141 permanent stations and 342 temporary stations (Figure 2a). We used the vertical component waveform data recorded from 2006 to 2017 to compute the noise cross-correlation functions (NCF) (Wang et al., 2018; Yao, 2012; Zheng et al., 2010). The processes mainly include resampling original data to 5 Hz, removing instrument response, removing mean and trend, band-pass filtering, spectral whitening, temporal normalization, and cross-correlation. Due to the long-time stack of daily NCFs, clear Rayleigh wave signals were obtained from the NCF (Figure 2c). Figure 3 displays the path coverage at four different periods. The azimuthal coverage is very good from short to intermediate periods (6–30 s) and is still quite good in the west of 108° at longer periods (40 s). Then we automatically picked the phase velocity dispersion curves with a method based on the imaging analysis technique (Yao et al., 2006, 2011). To eliminate some possible problems in the automatic method, we performed the quality control (Zhang et al., 2020) and path cluster analysis (Zhang et al., 2018, Figure in Supporting Information S1). Finally, we got 9,076 high-quality interstation Rayleigh wave phase velocity dispersion curves in the period range of 3–50 s Figure 2b shows the number of paths at different periods. We can notice that at most periods the path number is more than 3,000 and can reach 8,000 at intermediate periods (i.e., 14–20 s). At short (<10 s) and long (>40 s) periods there are still about 1,000 paths, which ensure a high-resolution tomography model in the SCB.

2.2. The Direct Inversion Method for 3-D Azimuthal Anisotropy

In this paper, we use the direct inversion method proposed by Liu et al. (2019), which can directly invert for 3-D Vs azimuthal anisotropy from Rayleigh wave phase velocity dispersion data. This method assumes the azimuthally anisotropic phase velocity variations are typically several percent in amplitude, which are much smaller than the isotropic phase velocity variations. Therefore, the forward calculation can use the fast-marching ray-tracing method by Rawlinson and Sambridge (2004) based only on the 2-D isotropic part phase velocities. Compared to the conventional two-step surface wave tomography method, the direct inversion method has two apparent advantages: (a) the two-step method is based on the individual inversion for the shear velocity model at each surface grid point and there is no constraint between adjacent grid points, while the direct inversion method can directly invert for the 3-D shear velocity structure with lateral and vertical model smoothness constraints; (b) based on the ray-tracing method, the direct inversion approach can consider the frequency-dependent ray-bending effect of surface waves in complex media and can efficiently improve the accuracy of surface wave inversion. The inversion procedure of this method can be divided into two stages: (a) in the first stage, the 3-D isotropic V_{sv} model is inverted directly from Rayleigh wave phase travel times (Fang et al., 2015); (b) after a reliable isotropic V_{sv} model is obtained, it is considered as an initial model in the second stage to invert for both 3-D V_{sv} azimuthal anisotropy and additional isotropic V_{sv} perturbations. Similar to previous surface wave tomography, the input data of the direct inversion method are still the Rayleigh wave phase velocity dispersion measurements of all ray paths. More details about this recently developed method can be found in Liu et al. (2019).

Considering the period band of dispersion curves, we mainly inverted for the shear wave velocity and azimuthal anisotropy structure of the crust and uppermost mantle in the study area, approximately from 0 to 70 km at depths. To obtain a good 3-D initial model, we combined three previous velocity models (Shen et al., 2016; Wang, Hubbard, et al., 2016; Zhang et al., 2020) in this area (see Supporting Information S1 and Figures S2 and S3 for the detailed information). The model grid size is 0.25° × 0.25° in the horizontal direction. Considering the decreasing resolution of surface waves with increasing depth, we give variable depth intervals instead of a fixed one. In the vertical direction, the grid size is therefore set as 3 km from depths of 0–15 km, and 5 km from depths of 15–50 km.

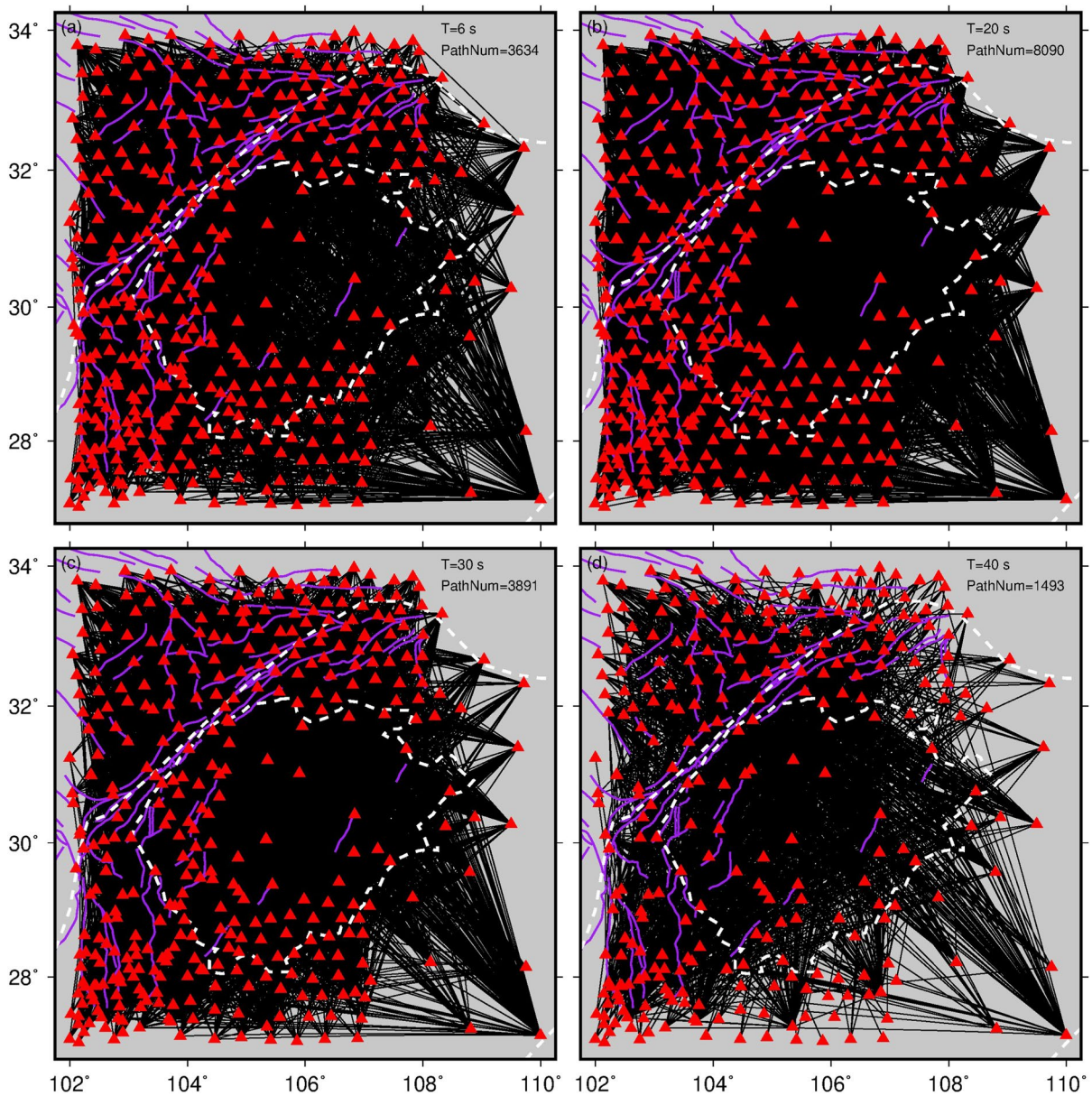

Figure 3. The path coverage at period 6, 20, 30, and 40 s. Red triangles are the stations, and black lines are the ray paths. "T" is the period, and "PathNum" is the path number at the corresponding period. Purple and white lines are the faults and block boundaries, as in Figure 1.

3. Results

3.1. Checkerboard and Reliability Tests

To analyze the resolution of the inversion method, we performed some checkerboard tests. We tested the checkerboard sizes of 0.6° × 0.6° and 0.8° × 0.8° patterns for isotropic and anisotropic anomalies, respectively. The isotropic velocity perturbation is ±5%, and the magnitude of azimuthal anisotropy is 2%. We added 0.5 s Gaussian random noise to the synthetic traveltime data. The model grid size is 0.2° × 0.2° in the horizontal direction. Other parameters are set the same as those in the inversion.

Figure 4 shows the recovered models of the isotropic and anisotropic anomalies, respectively. The 0.6° × 0.6° isotropic checkerboard pattern can be well recovered in the study area except the southeast and northeast corner (Figure 4e–4h). This is mainly due to lack of temporary stations in the eastern part of the study area (Figure 3). For the anisotropic anomalies, we can almost recover the 2% magnitude of anisotropy at the shallow depths

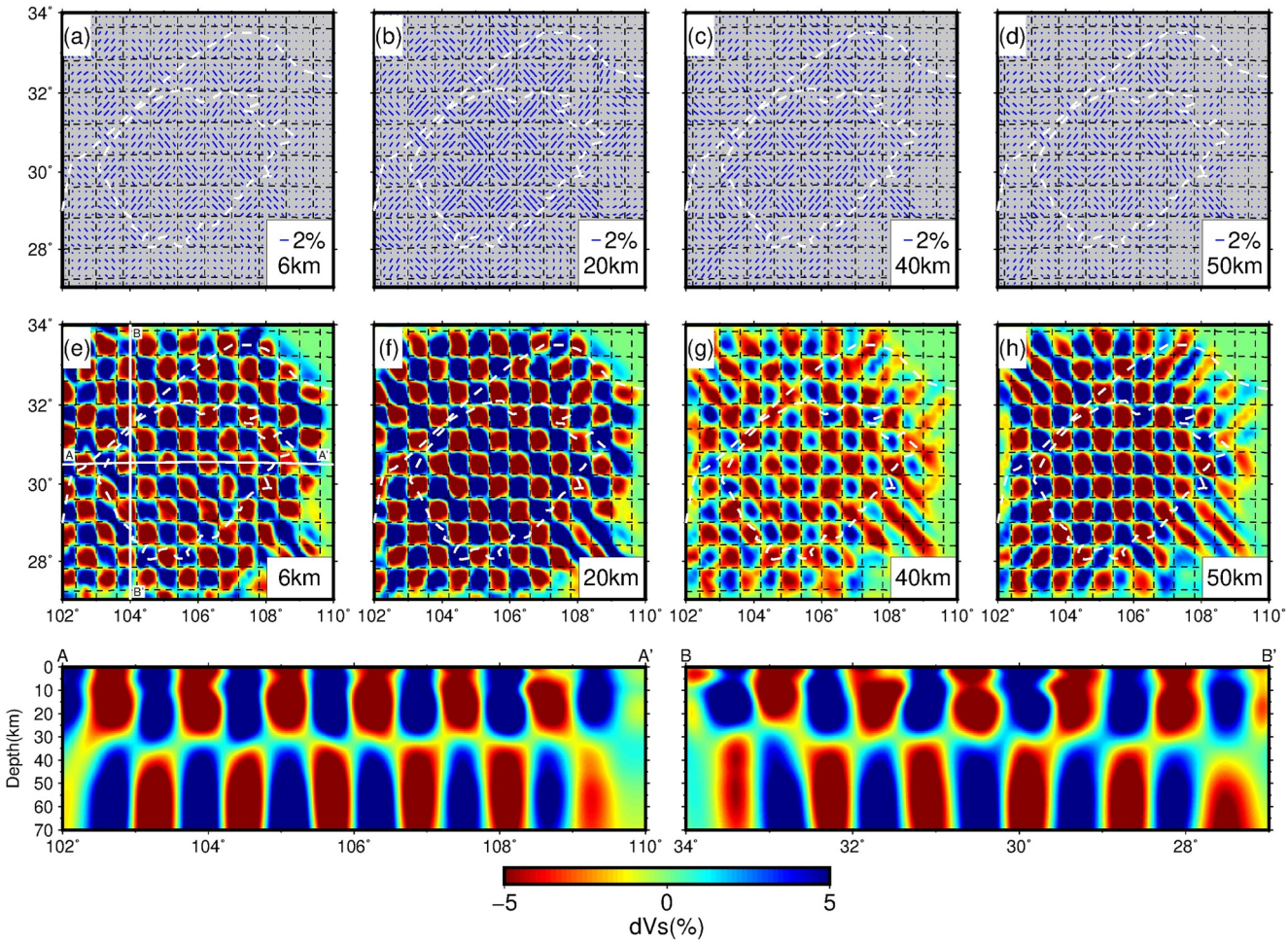

Figure 4. Results of checkerboard resolution tests. The velocity anomaly is 5% and the magnitude of azimuthal anisotropy is 2%. Black dashed lines in (a–h) show the boundary of true anisotropic and isotropic checkerboard pattern. The isotropic pattern is depth-dependent and changes after 30 km depth. (a–d) Recovered anisotropic models with the 0.8° × 0.8° checkerboard pattern. (e–h) Recovered isotropic models with the 0.6° × 0.6° checkerboard pattern. Profile AA' and BB' show the recovered isotropic models with the location marked as the white lines in (e).

(≤20 km) for the 0.8° × 0.8° checkerboard pattern (Figures 4a–4b). However, the recovered anisotropic models show smearing effects below 40 km depth, but we can still recover about 1% magnitude of anisotropic anomalies (Figures 4c–4d; see Figure S6 in Supporting Information S1 for the recovered results of depth-dependent anisotropic checkerboard test). We also conducted the synthetic tests for the trade-off between the isotropic and anisotropic patterns in the inversion, and the results show good reliability of the isotropic and anisotropic patterns in our inversion model (see Supporting Information S1 and Figures S7–S11 for the detailed information). However, due to the poor azimuthal coverage of dispersion data at longer period in the east (Figure 3c and 3d), the anisotropic pattern cannot be recovered in the east of 109° in the checkerboard (Figures 4c–4d, 4g, and 4h) and synthetic tests (see Supporting Information S1 and Figures S6, S9, and S11). Therefore, we will not show the anisotropic model in the east of 109° below 40 km depth.

3.2. 3-D Shear Wave Velocity and Azimuthal Anisotropy Structure

Figure 5 shows the isotropic shear wave velocity and azimuthal anisotropy structure from depths of 6–50 km. The inversion results using 3-D and 1-D initial models are quite similar (Figure S4 in Supporting Information S1), which indicates the stability of the 3-D direct inversion. The detailed information about the data fitting of the direct inversion is shown in Figure S5 in Supporting Information S1, which indicates a significant decrease of

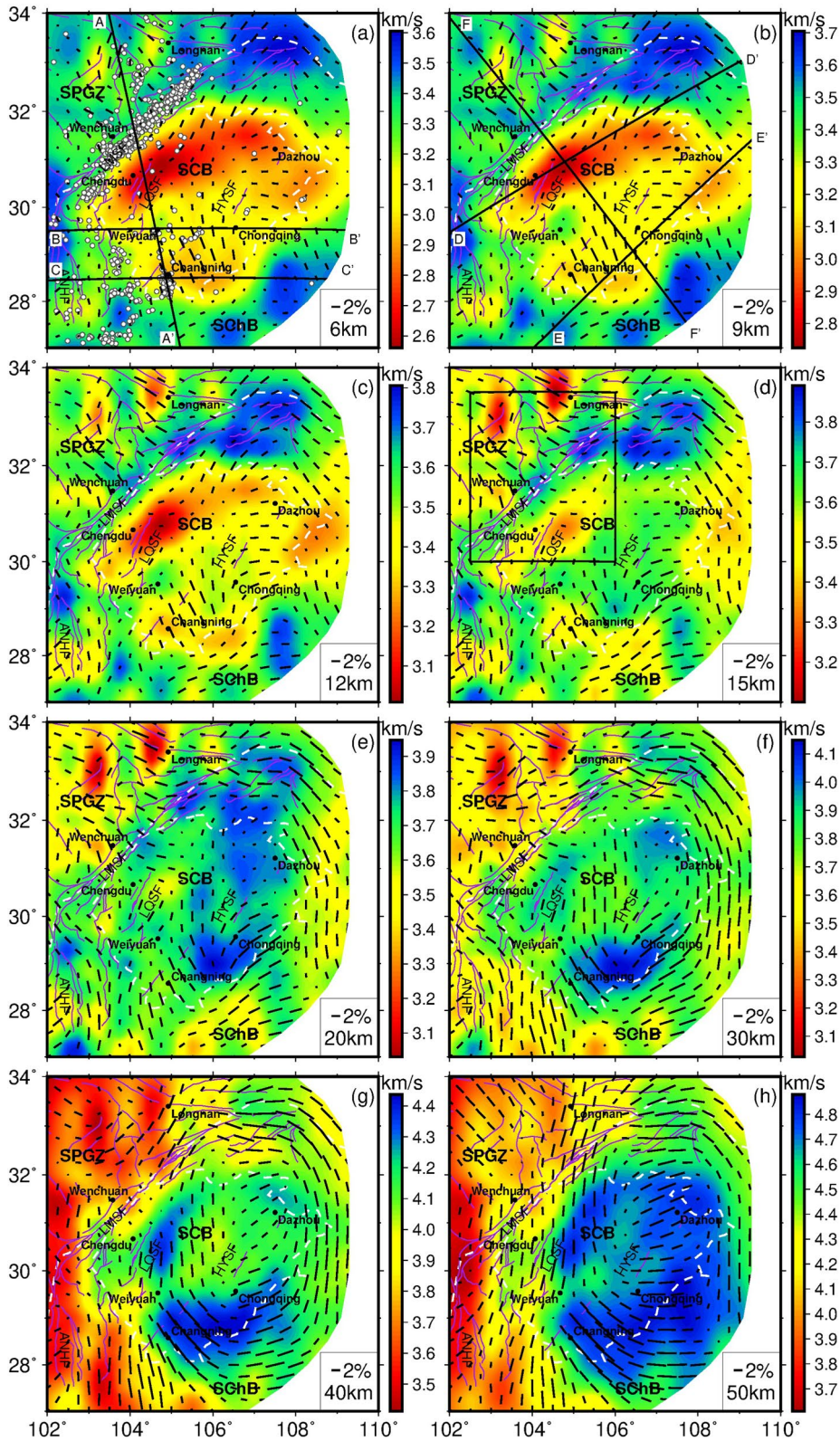

Figure 5. Shear wave velocity and azimuthal anisotropy model. Purple lines and dashed white lines are faults and block boundaries, respectively (the abbreviations of blocks and faults are the same as in Figure 1). Short black lines show the fast axis direction and magnitude of azimuthal anisotropy. Black dots are the major cities in this area. White dots in (a) are earthquakes with $M_w \geq 4.0$ since 1900 (collected from USGS, https://earthquake.usgs.gov).

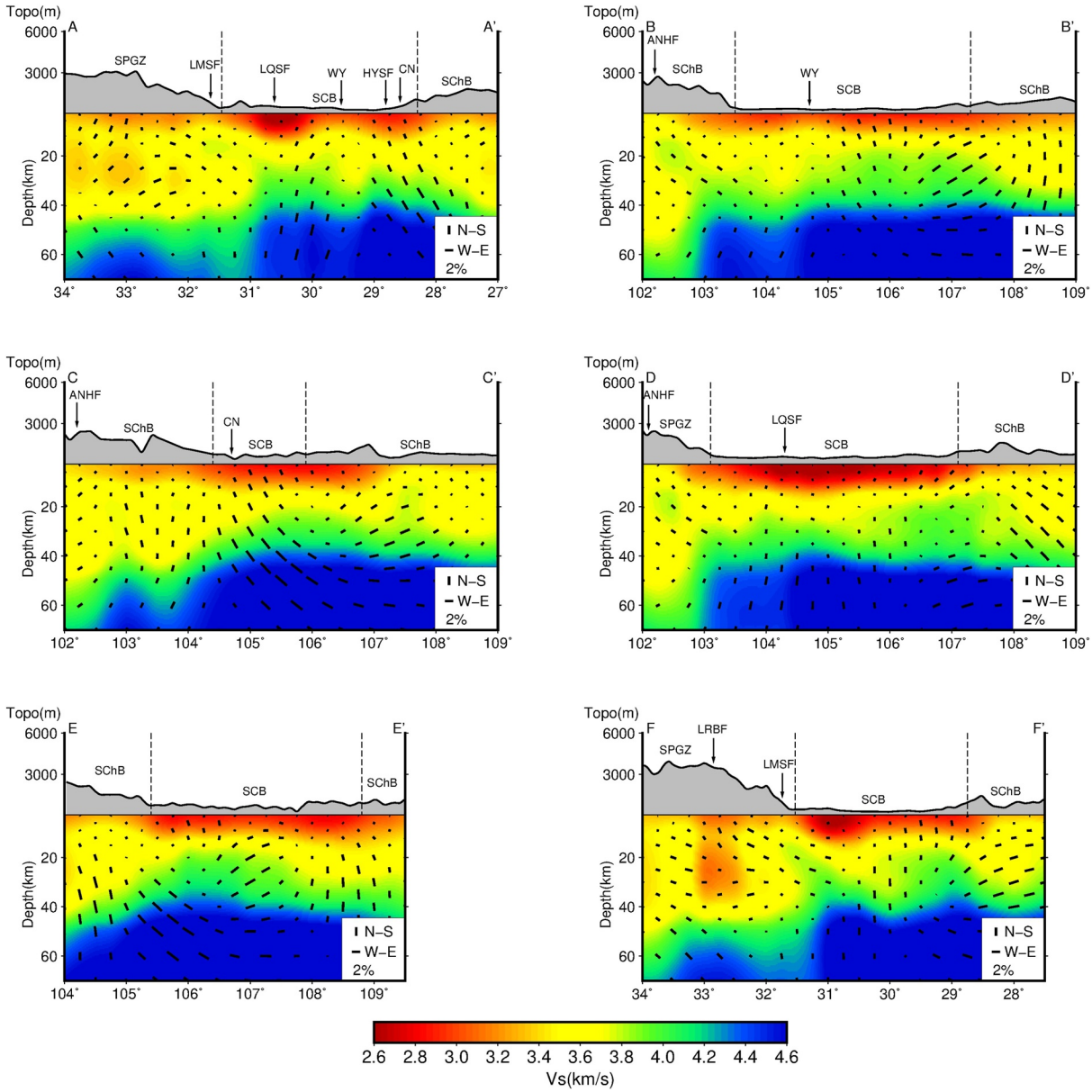

Figure 6. Vertical profiles of shear wave velocity and azimuthal anisotropy (profile AA'–FF') in the study area. The locations of the profiles are marked in Figures 4a and 4b. For each profile, the upper gray shaded part shows the topography. Dashed black lines and black arrows mark the boundary of blocks and the major faults and cities (WY, Weiyuan city; CN, Changning city), respectively. The abbreviations of blocks and faults are the same as in Figure 1. The lower part shows the velocity and anisotropy structure. Short black lines show the fast axis direction and magnitude of anisotropy in a geographic map view. The vertical bar and the horizontal bar in the bottom right corner represents the S-N fast direction and E-W fast direction of the azimuthal anisotropy, respectively.

the standard deviation of the traveltime residuals after the isotropic inversion and a continuing decrease of the standard deviation of the traveltime residuals after the isotropic and azimuthally anisotropic inversion.

At 6 km depth, there are two significant low-velocity anomalies in the SCB. One is mainly in the western Sichuan depression and the northern part of the central Sichuan uplift, whereas the other is mainly in the eastern Sichuan folds. Outside the SCB, most areas show high-velocity anomalies. From 9 to 15 km depths, the area of low-velocity anomalies inside the SCB gradually decreases. The low-velocity anomalies seem to extend to about 15 km depth and appear thicker in the western Sichuan depression than in the eastern Sichuan folds (profiles DD' and EE'in Figure 6). The central Sichuan uplift possesses a relatively strong high-velocity anomaly, especially in Weiyuan city at shallow depths (≤15 km). Below 20 km depth, the SCB changes to the high-velocity anomaly.

Low-velocity anomalies are mainly in the northwest of the LMSF and there are two obvious low-velocity anomalies near the Longriba fault and Longnan city, respectively. Below 40 km depth, a large-scale low-velocity anomaly widely presents in the west of the SCB, whereas the eastern SCB shows a strong high-velocity anomaly.

The azimuthal anisotropy shows a relatively weak variation in the vertical direction, but dramatic changes in the horizontal direction (Figures 5 and 6). The magnitude of anisotropy is weaker inside the SCB than the adjacent areas (Figures 5 and 6), which agrees well with previous azimuthal anisotropy results (Bao et al., 2020; Liang et al., 2020). The fast axis of the azimuthal anisotropy in the SPGZ maintains the NW-SE direction from 6 to 50 km depths but divides into two parts around the LMSF. In the northeastern part, the fast axis shows a rotational pattern and turns to nearly the E-W direction when crossing the Minshan fault. While in the southwestern part of the LMSF, the fast axis gradually turns to nearly the N-S direction. Azimuthal anisotropy patterns show little changes in the western Sichuan depression and central Sichuan uplift at all depths. The magnitude of anisotropy is very weak in the western Sichuan depression. The fast axis always shows nearly the N-S direction in the central Sichuan uplift. Notably, there are two earthquake swarms near Weiyuan and Changning cities, where also show strong contrast both on velocity anomaly and the fast axis direction (Figures 1b and 5a). The anisotropy patterns can be divided into two parts near Chongqing city in the eastern Sichuan folds. In the northeast of Chongqing, the fast axis shows nearly the NEE-SWW direction in the crust, and it gradually turns into the E-W direction at 50 km depth. However, the fast axis maintains the NW-SE direction at all depths in the southwest of Chongqing city. It is worth noticing that these two different anisotropy patterns in the eastern Sichuan folds are similar to the fast axis direction outside the SCB. In the southwestern corner of the study area, the fast axis always shows nearly the N-S direction, which is parallel to the strike of the Anninghe fault. Below 30 km depth, the fast axis seems always parallel to the strike of major strike-slip faults in the eastern margin of the SCB.

Figure 6 shows six profiles (AA'–FF') that cross the two low-velocity anomalies and the two earthquake swarms in the SCB. The location of these profiles is marked in Figures 5a–5b. From profiles AA'–CC', we notice that the low-velocity layer is relatively thin in the Weiyuan area, and the fast axis direction changes a lot from northwest in Weiyuan to southeast around Changning. The Weiyuan area shows weak azimuthal anisotropy, while the Changning area shows strong azimuthal anisotropy with the NW-SE fast axis direction. From profiles DD'and EE', we observe that the low-velocity anomaly in the western Sichuan depression and the northern part of the central Sichuan uplift extends to about 15 km depth, while the low-velocity anomaly in the eastern Sichuan folds only extends to about 12 km depth. In profiles AA' and FF', the approximate Moho depth derived by the velocity structure is about 40 km and the Moho interface appears very flat beneath the SCB, but it increases sharply to about 60 km depth when crossing the LMSF.

4. Discussion

4.1. The Sediments and Crustal Structure in Sichuan Basin

In the mid-upper crust ($\leq$15 km), we can notice that there are two obvious low-velocity anomalies in the northwestern and southeastern parts of the SCB, respectively. Petroleum and hydrologic exploration suggests the base of the Proterozoic section is about 12–15 km depths in the western Sichuan depression and eastern Sichuan folds (Wang, Hubbard, et al., 2016), which agrees well with the low-velocity anomalies inside the SCB in our model. We also notice that the low-velocity anomaly near the Longquanshan fault is the thickest, with a thickness of more than 15 km (Figures 5a–5e and profiles AA' and FF' in Figure 6). Its location is also close to the depocenter given by the sedimentary data (Meng et al., 2005). Therefore, the low-velocity anomalies are mainly caused by the thick sedimentary deposits in the SCB since the Sinian. The sediments in the western Sichuan depression may be related to the foreland subsidence that is mainly caused by the thrust of the LMSF (He et al., 2011; Wang, Hubbard, et al., 2016). However, the central Sichuan uplift shows a weak high-velocity anomaly in the upper crust. The absence of thick sediments in the central Sichuan uplift may be due to its relatively high elevation and far from the convergence boundary. The most significant high-velocity anomaly in the central Sichuan uplift is near Weiyuan city. The high-velocity anomaly may correspond to the Weiyuan anticline that consists of metasediments and igneous rocks (Wang, Hubbard, et al., 2016; Zeng et al., 2020).

Below 40 km depth, the high and low-velocity anomalies are mainly bounded by the LMSF and Anninghe fault. This velocity pattern is mainly caused by the difference in crustal thickness in the study area, while the possible crustal channel flow in the eastern margin of the plateau may enhance the low-velocity anomaly in the SPGZ

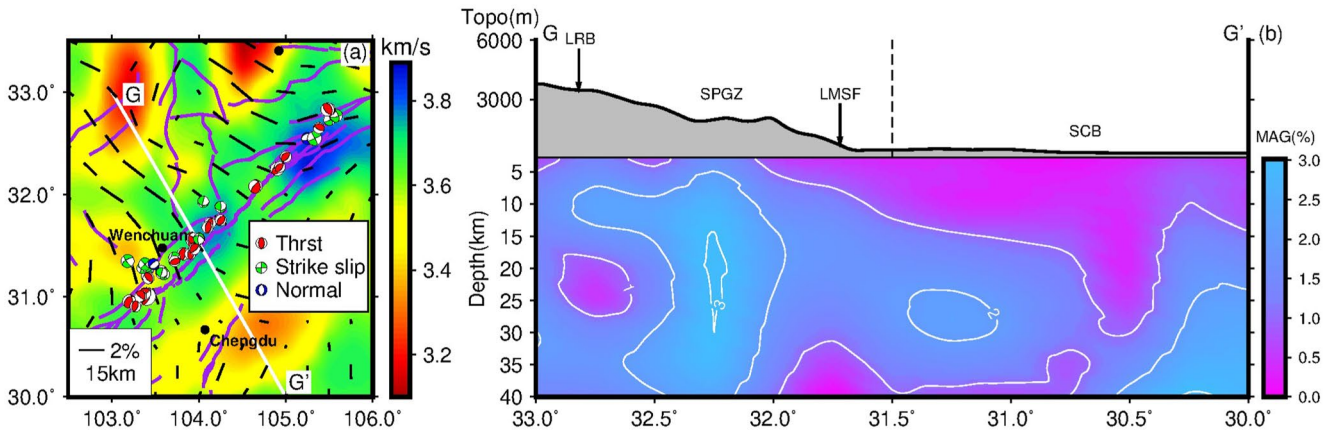

Figure 7. (a) Focal mechanisms of the 2008 Wenchuan earthquake sequence (from Hu et al., 2008) and the azimuthal anisotropy slice at 15 km depth. The background color shows the shear wave velocity. The region of this plot is marked by the black box in Figure 5d. (b) An azimuthal anisotropy profile crossing the LMSF, with the location of the profile marked in (a). The background color represents the magnitude of azimuthal anisotropy. The abbreviations of blocks and faults given above the topography (the top gray shaded area) are the same as in Figure 1.

(Feng et al., 2016; Wang, Hubbard, et al., 2016; Zhang et al., 2020). From the vertical profiles in Figure 6, the distribution of high velocity anomalies show strong contrast when crossing the LMSF. The strong lateral variations of high velocity anomalies in our velocity model agree well with the Moho depth obtained from seismic reflection profiles and receiver function studies (Feng et al., 2016; Li et al., 2018; Wang et al., 2017). Below 30 km depth, a high-velocity anomaly appears in the south part of SCB and gradually extends to the whole SCB, which is mainly due to the variation of Moho depths in the SCB. A seismic reflection profile detected a remnant of Neoproterozoic subduction beneath the central and western SCB (Gao et al., 2016), which may cause a slightly thicker crust in the northwestern SCB. The receiver function study (Wang et al., 2017) also revealed a thinner crust in the southern part of the SCB. Furthermore, there is a strong crustal low-velocity anomaly near the Longriba fault that extends to about 50 km depth (Figures 5c–5i and profile FF'in Figure 6), which is also revealed by the MT study (Zhao et al., 2019). The strong crustal low-velocity anomaly may be related to the viscoplastic materials that are extruded from the central Tibetan Plateau (Guo et al., 2015; Zhao et al., 2019).

4.2. The Deformation Inside the Sichuan Basin

Geologic factors that cause seismic anisotropy are often divided into two categories, that is, shape-preferred orientation (SPO) and lattice-preferred orientation (LPO). SPO is often related to the oriented cracks and layering of material in the upper crust. While LPO usually corresponds to the preferential alignment of mineral lattice such as mica or amphibole in the middle/lower crust and olivine in the upper mantle (Christensen, 1984; Crampin, 1981; Maupin & Park, 2007; Weiss et al., 1999). The orientation of cracks, layering, and mineral lattice are closely related to the regional stress and tectonic deformation history. Therefore, seismic anisotropy can be used to evaluate stress distribution, crustal and upper mantle deformation, and mantle flow processes effectively (Kong et al., 2016; Liang et al., 2020; Yao et al., 2010).

From Figure 5, we notice that the azimuthal anisotropy pattern can be divided into three parts inside the SCB and consistent with the sub-blocks of the SCB. The first part is in the western Sichuan depression. It shows very weak anisotropy from shallow crust to 40 km depth. From the obtained shear wave velocity model, the sediments in the western Sichuan depression are very thick. If the sediments did not experience intense deformation, it generally shows weak azimuthal anisotropy. Moreover, many previous studies suggest that the LMSF is a thrust fault with a right-lateral strike-slip component, and it displays a high-angle listric shape that dips 70° above 15 km depth and decreases to 30° gradually between the depth range of 15 and 22 km (Feng et al., 2016; Wang et al., 2014). Therefore, the high-angle listric fault is to transfer the horizontal extrusion from the SPGZ into the vertical displacement in the LMSF, which protects the western Sichuan depression from large-scale compressional deformation and provides a stable deposition environment. From Figure 7, we can clearly observe the change of magnitude of azimuthal anisotropy when crossing the LMSF. The magnitude of azimuthal anisotropy can reach 3% in the SPGZ but decrease sharply to less than 1% in the western Sichuan depression. However, below 15 km depth, the

magnitude of azimuthal anisotropy has a significant increase. This may be due to the low dip angle of the LMSF (about 30°) and its associated horizontal stress at this depth. But this horizontal stress does not seem to effectively transfer to the western Sichuan depression, which shows very weak azimuthal anisotropy (<1%, Figure 7b).

The second part is in the central Sichuan uplift. The anisotropy pattern changes little from 6 to 50 km depth. The fast axis always maintains nearly the N-S direction. This consistent anisotropy pattern may be due to the tectonic stability of the central Sichuan uplift, which is thought to have once been a microcontinent (Burchfiel et al., 1995; Xie & Zhang, 1982; Zhang et al., 2013). Therefore, the deformation is vertically coherent in the whole crust of the central Sichuan uplift. The N-S fast axis direction is not the same as the NE-SW trending of the central Sichuan uplift. Thus, we infer the N-S fast axis direction is the fossil anisotropy that was developed when the central Sichuan uplift was formed, and the anisotropy mainly preserved in mica and amphibole in the lower crust according to previous studies (Barruol & Mainprice, 1993; Weiss et al., 1999; Yao et al., 2010). Moreover, the compressive stress from the southeastward movement of the SPGZ and the northwestward extension of the Xuefeng intracontinental tectonic system have been absorbed by the LMSF (and the western Sichuan depression) and the eastern Sichuan folds, respectively, so that the interior of the central Sichuan uplift has not experienced deformation significantly. The collision of the South China Block and the North China Block in the late-Indosinia formed the Qinling-Dabie orogenic belt in the north of the central Sichuan uplift. However, the southward extension of the Qinling-Dabie orogenic belt has been offset due to the obstruction of the rigid Daba Mountain and the northwestern compressive stress from the Xuefeng intracontinental tectonic system, and formed a transition zone near the Dazhou city. The trumpetlike fold belts at the surface near the Dazhou city were caused by the opposite thrusting of these two different tectonic stresses (Figure 1a, Chen & Zhang, 1998; Zhang et al., 2013). Therefore, the weak anisotropy between Dazhou and Bazhong cities above 30 km depth reflects weak deformation in this area.

The third part is in the eastern Sichuan folds. The tectonic structures in the eastern Sichuan folds can be further divided into two styles: the arcuate structure in the northeast and the brush structure in the southwest (Chen & Zhang, 1998). We can see obvious fold belts with the NE-SW trending in the northeast of Chongqing in Figures 1a and 1b, which are mainly due to the extrusion of the northwestward extension of the Xuefeng intracontinental tectonic system (Tang et al., 2018; Zhang et al., 2013). Different from the relatively simple tectonic stress field in the northeast, the southwestern part of the eastern Sichuan folds has experienced multiple episodes of tectonic stress fields. Except for the NW trending stress from the Xuefeng intracontinental tectonic system until the late Palaeocence, the northward extrusion of the Dalou Mountain (Figure 1a) imposed the NS trending stress and formed the EW trending folds in the late Eocence. Then, the remote response of the collision between the Indian and Eurasian plates formed the EW trending stress in the early Oligocence. Nowadays, the increasing deformation strength of the Daliang Mountain led to the NE trending stress in this area (Tang et al., 2018). Therefore, the fast axis direction of azimuthal anisotropy is also very different in these two regions. In the northeast, the fast axis shows the NE-SW direction and is almost parallel to the trending of fold belts in this area. However, the fast axis exhibits the NW-SE direction in the southwest, which mainly due to the northeastward extrusion of the Daliang Mountain.

Furthermore, we notice that the azimuthal anisotropy pattern shows an apparent change near Weiyuan city. In the east, the fast axis shows nearly the N-S direction, while it changes to the NW-SE direction in the west (Figure 5 and profile AA' and BB' in Figure 6). Besides, the Weiyuan area shows a significant high-velocity anomaly in the shallow crust (≤15 km). Changning is located at the southwestern margin of the eastern Sichuan folds and also has strong seismicity after the exploration of shale gas in recent years. Similar to the Weiyuan area, the shear wave velocity structure and azimuthal anisotropy pattern both display strong contrast at shallow depths (≤15 km) in the Changning area (Figure 5 and profile AA' and CC' in Figure 6). These features indicate the heterogeneous tectonic stress distribution in these areas, which is also confirmed by previous studies (Wang, Huang, et al., 2016). Then the strong contrast in velocity structures may facilitate the accumulation of stress and strain (Mooney et al., 2012), thus more likely to induce earthquakes due to large regional stress variations during the shale gas exploration stage in these two areas (Ellsworth, 2013; Lei et al., 2019).

4.3. The Deformation Around the Sichuan Basin

Unlike the complex pattern of azimuthal anisotropy inside the SCB, the azimuthal anisotropy pattern is relatively simple around the SCB. The fast axis keeps NW-SE direction from 6 to 50 km depths in the SPGZ, which is mainly related to the southeastward movement and material transport in the SPGZ. However, the fast axis direction

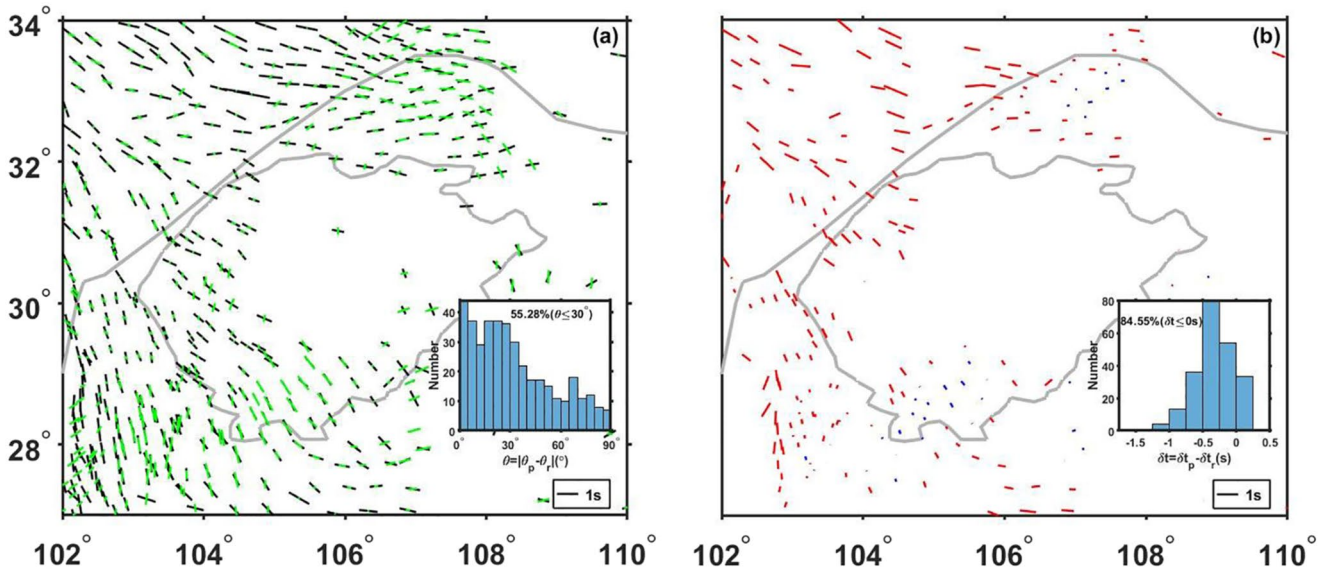

Figure 8. (a) The comparison between the predicted splitting parameters from our velocity model in the depth range of 0–50 km (green bars) and the observed splitting parameters from SKS data (black bars) (Chang et al., 2008, 2015, 2017) at stations in the study region. The inset shows the distribution of the fast axis angle difference (θ) between the predicted (θ_p) and observed (θ_r) splitting parameters. (b) The difference of delay time (δt) between the predicted (δt_p) and observed (δt_r) data with the angel difference between the predicted and observed splitting data less than 30°. Red bars represent δt less than 0 s and blue bars represent δt larger than 0 s. The inset shows the distribution of δt. Gray lines show the main block boundaries.

changes to two different patterns when reaching the LMSF (Figures 5a–5g and Figure 7a). The NW-SE fast axis direction changes to nearly the E-W direction in the northeastern part of the LMSF in the upper and middle crust and nearly the N-S direction in the southwestern part of the LMSF from the upper to lower crust. This indicates the southeastward movement of the SPGZ has been obstructed by the rigid SCB and then the movement of materials is bifurcated along the LMSF. Moreover, the focal mechanisms also show strike-slip features in the two ends and thrust in the central part of the LMSF (Figure 7a, Hu et al., 2008, 2012; Zheng et al., 2009). Then the fast axis has a nearly NS direction in the southwestern corner of the study area, which is closely related to the simple shear of the N-S trending left-lateral strike-slip Anninghe fault.

Remarkably, the fast axis is almost parallel to the margin of the SCB in the eastern area from 15 km depth. The fast axis has a NE-SW direction in the southeast and a NW-SE direction in the northeast, while the anisotropy is relatively weak inside the SCB. Field observations find many strike-slip faults in the eastern margin of the SCB, suggesting that the SCB has experienced right-lateral shear along its margin (Wang et al., 2014). Paleomagnetic data (Tong et al., 2019, 2020) also suggest that the SCB may experience block rotation. Although the eastern margin of the SCB is affected by the extrusion of the Xuefeng intracontinental tectonic system and the Daliang Mountain, strike-slip faults in this area may transform the compressive stress to shear deformation in the crust.

Below 40 km depth, the ring shape fast axis direction may be mainly due to extrusion of adjacent areas is obstructed by the rigid SCB and caused pure-shear deformation around the eastern margin. Then the pure-shear deformation formed the ring shape lattice-preferred orientation of olivine (Christensen, 1984; Kaminski & Ribe, 2001; Mainprice et al., 2005; Maupin & Park, 2007) in the uppermost mantle of the eastern margin of the SCB.

4.4. Comparison With Shear Wave Splitting Measurements

Teleseismic shear wave splitting measurements using SKS and SKKS phases have been widely used to understand the deformation of lithosphere and asthenosphere in the world (Savage, 1999; Silver, 1996). However, this type of measurements usually lacks vertical resolution compared to the depth-dependent seismic anisotropy obtained from surface wave tomography. Here we also compare our azimuthal anisotropy pattern with the teleseismic shear wave splitting results (Chang et al., 2008, 2015, 2017). The azimuthal anisotropy determined in our study shows similar patterns with the shear wave splitting results mainly in the regions of SPGZ, southern margin of the SCB, and the Anninghe fault zone area (Figures 8 and 9).

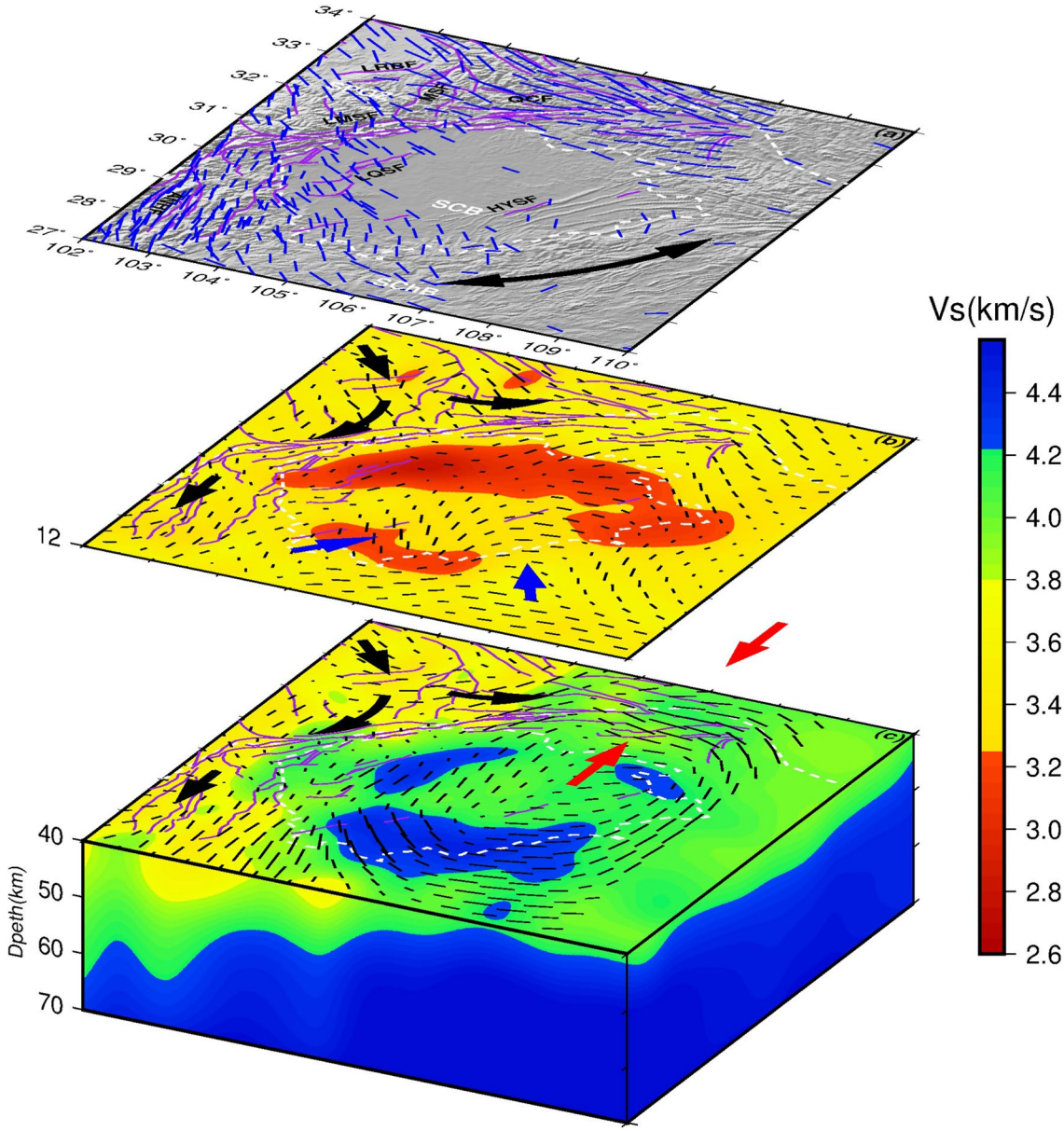

Figure 9. Perspective view of 3-D shear wave velocity and azimuthal anisotropy model for the Sichuan Basin and its adjacent areas. Purple and white lines are the faults and block boundaries (see Figure 1 in detail). In (a), blue short lines indicate the fast axes determined by teleseismic shear wave splitting analysis (Chang et al., 2008, 2015, 2017). Double-head black arrows show the possible rotation in the southeast of the Sichuan Basin (Tong et al., 2019; Wang et al., 2014). In (b) and (c), short black lines represent the azimuthal anisotropy, and the background color shows shear wave velocity. Black arrows represent the possible movement direction of the crustal materials, blue and red arrows show the possible compressive stress distribution derived from the anisotropy pattern and tectonic history.

Similarly as Yao et al. (2010) we calculated the predicted teleseismic shear wave splitting parameters from our azimuthally anisotropic shear velocity model from surface to 50 km depth according to the formulas proposed by Montagner et al. (2000). Figure 8 shows the comparsion between predicted and the observed splitting parameters at stations in our study region. The predicted shear wave splitting show good coherence with the observed SKS splitting (Figure 8a). The percentage of fast axis angel difference (θ) between the predicted (θ_p) and observed (θ_r) splitting data less than 30° is about 55% (the inset of Figure 8a). For those stations with the fast axis angel difference between the predicted and observed splitting data less than 30°, the percentage of the difference of delay time (δt) between the predicted (δt_p) and observed (δt_r) data less than 0 s is about 85% (the inset of Figure 8b), which shows systematically smaller predicted delay times than the observed ones. At some stations in the southern SCB, the observed splitting time is less than the predicted one from the crust and uppermost mantle

anisotropy, which is probably due to the existence of complex and depth-varying azimuthal anisotropy in the upper mantle that makes the total teleseismic splitting time smaller. At some stations inside the SCB, we observe very different fast directions predicted from our model and the observed teleseismic splitting. This indicates apparent depth-dependent azimuthal anisotropy patterns in the crust and upper mantle, probably due to the multistage deformation history of the SCB.

Splitting parameters inferred from receiver functions and local events (Gao et al., 2018; Zheng et al., 2018), which mainly reflect the average azimuthal anisotropy of the part of (or entire) crust, show similar fast directions with the predicted splitting data in the SPGZ and the Anninghe-Dalingshan fault zone area. The similar splitting parameters from different types of data indicate that crustal azimuthal anisotropy has a significant contribution to teleseismic shear wave splitting measured in these regions (Sun et al., 2012; Yao et al., 2010). The δt is large in the region north or northwest of the SCB (Figure 8b). Previous studies (Guo & Chen, 2017; Shen et al., 2017) suggest that an eastward mantle flow may exist beneath the Qinling orogenic belt, north of the SCB. The eastward mantle flow may also form E-W trending anisotropy. Therefore, the teleseismic splitting may have contributions from both crustal and upper mantle anisotropy in the region north or northwest of the SCB, and the mantle flow may be the predominant source for the observed azimuthal anisotropy.

4.5. Multi-Stage Deformation Processes of the Sichuan Basin

The SCB and its marginal area have undergone complicated multi-stage tectonic evolution (He et al., 2011; Tang et al., 2018; Xie & Zhang, 1982; Zhang et al., 2013) since it is located in the convergence zone of the South China Block, North China Block, and Songpan-Ganzi Block. The central Sichuan continent and the Yangtze Craton may be pieced together in the late Mesoproterozoic, which produced the fossil anisotropy of the central Sichuan uplift that continues to the present. Since the Sinian, the South China Block was in a stretching stage due to the influence of the break-off of the Rodinia supercontinent. The Yangtze and Cathaysia Blocks were separated and formed a rift basin in the Jiangnan-Xuefeng area. In the late Ordovician, however, the Yangtze and Cathaysia Blocks pieced together again and the South China Block went into the intercontinental orogeny stage. This intercontinental orogeny generated SE-NW tectonic stresses in the Jiangnan-Xuefeng area and caused uplift of this area and formation of the prototype of the Xuefeng intracontinental tectonic system. Meanwhile, the Qinling paleooceanic basin began to subduct beneath the North China Block and drag the South China Block to move northward.

In the Indosinian stage, the oceanic basin around the Yangtze Block had subducted. The Qiangtang Block, Songpan-Ganzi Block, and North China Block collided with the South China Block in the western margin. The N-S trending collision of the North China Block and South China Block formed the Qinling-Dabie orogenic belt and caused the nearly E-W trending lattice-preferred orientation of olivine in the uppermost mantle of the northeastern margin of SCB (red arrows in Figure 9c). The interaction between the Songpan-Ganzi Block and South China Block formed the Longmenshan orogenic belt and turned the western Sichuan depression into a foreland basin. In the east of the South China Block, the intercontinental orogeny had influenced the western margin of the Xuefeng Mountain, which facilitated the formation of the Xuefeng intracontinental tectonic system. The tectonic deformation of the Xuefeng intracontinental tectonic system reached the Huayingshan fault in the late Cretaceous. The new deformation from the Xuefeng intracontinental tectonic system may override the former deformation and cause the NE-SW trending crustal anisotropy in eastern Sichuan folds (blue arrows in Figure 9b).

In the Cenozoic, the collision of the Indian and Eurasian plates caused the thickening of the Songpan-Ganzi Block and the rise of Longmenshan again. At this time, the present tectonic pattern around the SCB was basically formed. The southeastward crustal extrusion in the Songpan-Ganzi Block may form the NW-SE trending anisotropy and the extrusion was bifurcated along the LMSF due to the obstruction of the rigid SCB (black arrows in Figures 9b and 9c). Meanwhile, the remote response of the collision of Indian and Eurasian plates enhanced the tectonic deformation of the Daliang Mountain (blue arrows in Figure 9b), influenced the southwestern part of eastern Sichuan folds, and formed the NW-SE trending crustal anisotropy.

5. Conclusions

We used ambient noise dispersion data from 483 seismic stations in the SCB and its adjacent area to directly invert for the high-resolution 3-D shear wave velocity and azimuthal anisotropy model. From the model, we obtained the following major conclusions.

1. There are very thick sediments in the western Sichuan depression and eastern Sichuan folds, but little sediments in the central Sichuan uplift. The magnitude of anisotropy is very weak in the western Sichuan depression. The central Sichuan uplift is used to be a microcontinent and lacks of deformation after its formation, thus showing relatively strong and coherent fossil anisotropy.
2. Two different anisotropy patterns in the eastern Sichuan folds were caused by the northwestward extension of the Xuefeng intracontinental tectonic system and the northeastward extrusion of the Daliang Mountain, respectively.
3. The anisotropy pattern displays an apparent change near the Weiyuan and Changning regions, which indicates the heterogeneous tectonic stress distribution in these areas, thus facilitating strain accumulation and earthquake generation.
4. The changes of fast axis directions around the LMSF are related to the resistance of the SCB to the southeastward extrusion of viscoplastic materials from the central plateau to the two ends of the LMFS. The obstruction of the rigid SCB and strike-slip faults transform the compressive stress to shear deformation and cause the fast axis direction parallel to the eastern margin of the SCB.

Conflict of Interest

The authors declare no conflicts of interest relevant to this study.

Data Availability Statement

The continuous waveform data were provided by Data Management Centre of China National Seismic Network at Institute of Geophysics, China Earthquake Administration (doi:10.11998/SeisDmc/SN, http://www.seisdmc.ac.cn). The dispersion data and the final 3-D shear wave velocity and azimuthal anisotropy model can be accessed at https://doi.org/10.5281/zenodo.4678179.

Acknowledgments
The authors acknowledge Dr. Lijun Chang from Institute of Geophysics, China Earthquake Administration, for providing the shear wave splitting data for comparison with our results. This work is supported by National Key R&D Program of China (2018YFC1503400), the Special Fund of the Institute of Geophysics, China Earthquake Administration (grants no. DQJB21Z03), the Natural National Science Foundation of China (41790464, 41790463), the LU JIAXI International team program supported by the KC Wong Education Foundation, and CAS (GJTD-2018-12).

References

Bao, X., Song, X., David, W. E., Xu, Y., & Chen, H. (2020). Episodic lithospheric deformation in eastern Tibet inferred from seismic anisotropy. *Geophysical Research Letters*, *47*, e2019GL085721. https://doi.org/10.1029/2019gl085721

Barruol, G., & Mainprice, D. (1993). 3-D seismic velocities calculated from lattice-preferred orientation and reflectivity of a lower crustal section: Examples of the Val Sesia section (Ivrea Zone, Northern Italy). *Geophysical Journal International*, *115*, 1169–1188. https://doi.org/10.1111/j.1365-246X.1993.tb01519.x

Burchfiel, B. C., Chen, Z., Liu, Y., & Royden, L. H. (1995). Tectonics of the Longmen Shan and adjacent regions, Central China. *International Geology Review*, *37*, 661–735. https://doi.org/10.1080/00206819509465424

Chang, L., Ding, Z., & Wang, C. (2015). Upper mantle anisotropy beneath the southern segment of North-South tectonic belt, China. *Chinese Journal of Geophysics*, *58*, 4052–4067. https://doi.org/10.1007/s11430-015-5098-2

Chang, L., Ding, Z., Wang, C., & Flesch, L. M. (2017). Vertical coherence of deformation in lithosphere in the NE margin of the Tibetan plateau using GPS and shear-wave splitting data. *Tectonophysics*, *699*, 93–101. https://doi.org/10.1016/j.tecto.2017.01.025

Chang, L., Wang, C., & Ding, Z. (2008). Seismic anisotropy of upper mantle in Sichuan and adjacent regions. *Science in China - Series D: Earth Sciences*, *51*, 1683–1693. https://doi.org/10.1007/s11430-008-0147-8

Chen, M., & Zhang, S. (1998). Characteristics and forming mechanism of opposite protruding arcuate structural zones in the thress gorges area of the Yangtze River, South China. *Geology and Mineral Resources of South China*, *1*, 3–5.

Christensen, N. I. (1984). The magnitude, symmetry and origin of upper mantle anisotropy based on fabric analyses of ultramafic tectonites. *Geophysical Journal of the Royal Astronomical Society*, *76*, 89–111. https://doi.org/10.1111/j.1365-246X.1984.tb05025.x

Crampin, S. (1981). A review of wave motion in anisotropic and cracked elastic-media. *Wave Motion*, *3*, 343–391. https://doi.org/10.1016/0165-2125(81)90026-3

Ellsworth, W. L. (2013). Injection-induced earthquakes. *Science*, *341*, 143. https://doi.org/10.1126/science.1225942

Fang, H., Yao, H., Zhang, H., Huang, Y.-C., & van der Hilst, R. D. (2015). Direct inversion of surface wave dispersion for three-dimensional shallow crustal structure based on ray tracing: Methodology and application. *Geophysical Journal International*, *201*, 1251–1263. https://doi.org/10.1093/gji/ggv080

Feng, S., Zhang, P., Liu, B., Wang, M., Zhu, S., Ran, Y., et al. (2016). Deep crustal deformation of the Longmen Shan, eastern margin of the Tibetan Plateau, from seismic reflection and Finite Element modeling. *Journal of Geophysical Research*, *121*, 767–787. https://doi.org/10.1002/2015jb012352

Gao, R., Chen, C., Wang, H., Lu, Z., Brown, L., Dong, S., et al. (2016). SINOPROBE deep reflection profile reveals a Neo-Proterozoic subduction zone beneath Sichuan Basin. *Earth and Planetary Science Letters*, *454*, 86–91. https://doi.org/10.1016/j.epsl.2016.08.030
Gao, Y., Shi, Y., & Chen, A. (2018). Crustal seismic anisotropy and compressive stress in the eastern margin of the Tibetan Plateau and the influence of the M_S8.0 Wenchuan earthquake. *Chinese Science Bulletin*, *63*, 1934–1948. https://doi.org/10.1360/n972018-00317
Guo, X., Gao, R., Xu, X., Keller, G. R., Yin, A., & Xiong, X. (2015). Longriba fault zone in eastern Tibet: An important tectonic boundary marking the westernmost edge of the Yangtze block. *Tectonics*, *34*, 970–985. https://doi.org/10.1002/2015tc003880
Guo, Z., & Chen, Y. J. (2017). Mountain building at northeastern boundary of Tibetan Plateau and craton reworking at Ordos block from joint inversion of ambient noise tomography and receiver functions. *Earth and Planetary Science Letters*, *463*, 232–242. https://doi.org/10.1016/j.epsl.2017.01.026
He, D., Li, D., Zhang, G., Zhao, L., Fan, C., Lu, R., & Wen, Z. (2011). Formation and evolution of multi-cycle superposed Sichuan Basin, China. *Chinese Journal of Geology*, *46*, 589–606.
He, D., Lu, R., Huang, H., Wang, X., Jiang, H., & Zhang, W. (2019). Tectonic and geological background of the earthquake hazards in Changning shale gas development zone, Sichuan Basin, SW China. *Petroleum Exploration and Development*, *46*, 993–1006. https://doi.org/10.1016/s1876-3804(19)60262-4
Hu, X., Cui, X., Ning, J., & Chen, L. (2012). Preliminary study on tectonic deformation models in the Longmenshan region based on focal mechanism solutions of the Wenchuan earthquake sequence. *Chinese Journal of Geophysics*, *55*, 2561–2574.
Hu, X., Yu, C., Tao, K., Cui, X., Ning, J., & Wang, Y. (2008). Focal mechanism solutions of Wenchuan earthquake and its strong aftershocks obtained from initial P wave polarity analysis. *Chinese Journal of Geophysics*, *51*, 1711–1718.
Kaminski, E., & Ribe, N. M. (2001). A kinematic model for recrystallization and texture development in olivine polycrystals. *Earth and Planetary Science Letters*, *189*, 253–267. https://doi.org/10.1016/s0012-821x(01)00356-9
Kang, Y. (2014). Types and evolution characteristics of global sedimentary basins. *Natural Gas Industry*, *34*, 10–18.
Kong, F., Wu, J., Liu, K. H., & Gao, S. S. (2016). Crustal anisotropy and ductile flow beneath the eastern Tibetan Plateau and adjacent areas. *Earth and Planetary Science Letters*, *442*, 72–79. https://doi.org/10.1016/j.epsl.2016.03.003
Lei, X., Wang, Z., & Su, J. (2019). The December 2018 ML 5.7 and January 2019 ML 5.3 earthquakes in south Sichuan Basin induced by shale gas hydraulic fracturing. *Seismological Research Letters*, *90*, 1099–1110. https://doi.org/10.1785/0220190029
Li, J., Shi, B., Xu, X., & Hu, J. (2018). Crustal structure beneath the Sichuan basin and adjacent regions revealed by teleseismic receiver functions. *Chinese Journal of Geophysics*, *61*, 2719–2735.
Liang, C., Liu, Z., Hua, Q., Wang, L., Jiang, N., & Wu, J. (2020). The 3D seismic azimuthal anisotropies and velocities in the eastern Tibetan Plateau extracted by an azimuth-dependent dispersion curve inversion method. *Tectonics*, *39*, e2019TC005747. https://doi.org/10.1029/2019tc005747
Liu, C., Yao, H., Yang, H.-Y., Shen, W., Fang, H., Hu, S., & Qiao, L. (2019). Direct inversion for three-dimensional shear wave speed azimuthal anisotropy based on surface wave ray tracing: Methodology and application to Yunnan, southwest China. *Journal of Geophysical Research*, *124*, 11394–11413. https://doi.org/10.1029/2018jb016920
Mainprice, D., Tommasi, A., Couvy, H., Cordier, P., & Frost, D. J. (2005). Pressure sensitivity of olivine slip systems and seismic anisotropy of Earth's upper mantle. *Nature*, *433*, 731–733. https://doi.org/10.1038/nature03266
Maupin, V., & Park, J. (2007). Theory and observations: Seismic anisotropy. In G. Schubert (Ed.), *Treatise on geophysics* (pp. 277–305). Elsevier.
Meng, Q. R., Wang, E., & Hu, J. M. (2005). Mesozoic sedimentary evolution of the northwest Sichuan basin: Implication for continued clockwise rotation of the South China block. *The Geological Society of America Bulletin*, *117*, 396–410. https://doi.org/10.1130/b25407.1
Montagner, J. P., Griot-Pommera, D. A., & Lave, J. (2000). How to relate body wave and surface wave anisotropy? *Journal of Geophysical Research*, *105*, 19015–19027. https://doi.org/10.1029/2000jb900015
Mooney, W. D., Ritsema, J., & Hwang, Y. K. (2012). Crustal seismicity and the earthquake catalog maximum moment magnitude (M-Cmax) in stable continental regions (SCRs): Correlation with the seismic velocity of the lithosphere. *Earth and Planetary Science Letters*, *357*, 78–83. https://doi.org/10.1016/j.epsl.2012.08.032
Rawlinson, N., & Sambridge, M. (2004). Wave front evolution in strongly heterogeneous layered media using the fast marching method. *Geophysical Journal International*, *156*, 631–647. https://doi.org/10.1111/j.1365-246X.2004.02153.x
Savage, M. K. (1999). Seismic anisotropy and mantle deformation: What have we learned from shear wave splitting? *Reviews of Geophysics*, *37*, 65–106. https://doi.org/10.1029/98rg02075
Shen, W., Ritzwoller, M. H., Kang, D., Kim, Y., Lin, F., Ning, J., et al. (2016). A seismic reference model for the crust and uppermost mantle beneath China from surface wave dispersion. *Geophysical Journal International*, *206*, 954–979. https://doi.org/10.1093/gji/ggw175
Shen, X., Liu, M., Gao, Y., Wang, W., Shi, Y., An, M., et al. (2017). Lithospheric structure across the northeastern margin Plateau: Implications for the plateau's lateral growth. *Earth and Planetary Science Letters*, *459*, 80–92. https://doi.org/10.1016/j.epsl.2016.11.027
Silver, P. G. (1996). Seismic anisotropy beneath the continents: Probing the depths of geology. *Annual Review of Earth and Planetary Sciences*, *24*, 385–432. https://doi.org/10.1146/annurev.earth.24.1.385
Sun, Y., Niu, F., Liu, H., Chen, Y., & Liu, J. (2012). Crustal structure and deformation of the SE Tibetan plateau revealed by receiver function data. *Earth and Planetary Science Letters*, *349*, 186–197. https://doi.org/10.1016/j.epsl.2012.07.007
Tang, Y., Zhou, L., Chen, K., Dong, X., & Tang, W. (2018). Analysis of tectonic stress field of Southeastern Sichuan and formation mechanism of tectonic deformation. *Geological Review*, *64*, 15–28.
Tong, Y., Sun, Y., Wu, Z., Mao, C., Pei, J., Yang, Z., et al. (2019). Passive crustal clockwise rotational deformation of the Sichuan Basin since the Miocene and its relationship with the tectonic evolution of the fault systems on the eastern edge of the Tibetan Plateau. *The Geological Society of America Bulletin*, *131*, 175–190. https://doi.org/10.1130/b31965.1
Tong, Y., Wu, Z., Sun, Y., Yang, Z., Pei, J., Yang, X., et al. (2020). The interaction of the eastward extrusion of the Songpan-Ganzi Terrane and the crustal rotational movement of the Sichuan Basin since the late Paleogene: Evidence from Cretaceous and Paleogene Paleomagnetic data sets of the Sichuan Basin. *Tectonics*, *39*, e2019TC005784. https://doi.org/10.1029/2019tc005784
Wang, C., Yang, W., Wu, J., & Ding, Z. (2015). Study on the lithospheric structure and earthquakes in North-South tectonic belt. *Chinese Journal of Geophysics*, *58*, 3867–3901.
Wang, E., Meng, K., Su, Z., Meng, Q., Chu, J. J., Chen, Z., et al. (2014). Block rotation: Tectonic response of the Sichuan basin to the southeastward growth of the Tibetan Plateau along the Xianshuihe-Xiaojiang fault. *Tectonics*, *33*, 686–717. https://doi.org/10.1002/2013tc003337
Wang, M., Hubbard, J., Plesch, A., Shaw, J. H., & Wang, L. (2016). Three-dimensional seismic velocity structure in the Sichuan basin, China. *Journal of Geophysical Research*, *121*. https://doi.org/10.1002/2015JB012644
Wang, M., Yang, H., Fang, L., Han, L., Jia, D., Jiang, D., & Yan, B. (2020). Shallow faults reactivated by hydraulic fracturing: The 2019 Weiyuan earthquake sequences in Sichuan, China. *Seismological Research Letters*, *91*, 3171–3181. https://doi.org/10.1785/0220200174
Wang, W., Wang, B., & Zheng, X. (2018). Public cloud computing for seismological research: Calculating large-scale noise cross-correlations using ALIYUN. *Earthquake Science*, *31*, 227–233. https://doi.org/10.29382/eqs-2018-0227-2

Wang, W., Wu, J., Fang, L., Lai, G., & Cai, Y. (2017). Crustal thickness and Poisson's ratio in southwest China based on data from dense seismic arrays. *Journal of Geophysical Research*, *122*, 7219–7235. https://doi.org/10.1002/2017jb013978

Wang, Y., Huang, J., Wang, S., Dong, D., Zhang, C., & Guan, Q. (2016). Dissection of two calibrated areas of the Silurian Longmaxi formation, changning and Jiaoshiba, Sichuan Basin. *Natural Gas Geoscience*, *27*, 423–432.

Wei, G., Chen, G., Du, S., Zhang, L., & Yang, W. (2008). Petroleum systems of the oldest gas field in China: Neoproterozoic gas pools in the Weiyuan gas field, Sichuan Basin. *Marine and Petroleum Geology*, *25*, 371–386. https://doi.org/10.1016/j.marpetgeo.2008.01.009

Weiss, T., Siegesmund, S., Rabbel, W., Bohlen, T., & Pohl, M. (1999). Seismic velocities and anisotropy of the lower continental crust: A review. *Pure and Applied Geophysics*, *156*, 97–122. https://doi.org/10.1007/s000240050291

Xie, Q., & Zhang, Z. (1982). The formation of "central Sichuan microcontinent" and Sichuan Basin. *Acta Geologica Sichuan*, *3*, 50–53.

Yao, H. (2012). Lithospheric structure and deformation in SE Tibet revealed by ambient noise and earthquake surface wave tomography: Recent advances and perspectives. *Earthquake Science*, *25*, 371–383. https://doi.org/10.1007/s11589-012-0863-1

Yao, H., Gouedard, P., Collins, J. A., McGuire, J. J., & van der Hilst, R. D. (2011). Structure of young East Pacific Rise lithosphere from ambient noise correlation analysis of fundamental- and higher-mode Scholte-Rayleigh waves. *Comptes Rendus Geoscience*, *343*, 571–583. https://doi.org/10.1016/j.crte.2011.04.004

Yao, H., van der Hilst, R. D., & de Hoop, M. V. (2006). Surface-wave array tomography in noise and two-station analysis - I. SE Tibet from ambient seismic phase velocity maps. *Geophysical Journal International*, *166*, 732–744. https://doi.org/10.1111/j.1365-246X.2006.03028.x

Yao, H., van der Hilst, R. D., & Montagner, J.-P. (2010). Heterogeneity and anisotropy of the lithosphere of SE Tibet from surface wave array tomography. *Journal of Geophysical Research*, *115*. https://doi.org/10.1029/2009jb007142

Zeng, Q., Chu, R., Sheng, M., & Wei, Z. (2020). Seismic ambient noise tomography for shallow velocity structures beneath Weiyuan, Sichuan. *Chinese Journal of Geophysics*, *63*, 944–955

Zhang, G., Guo, A., Wang, Y., Li, S., Dong, Y., Liu, S., et al. (2013). Tectonics of South China continent and its implications. *Science China Earth Sciences*, *56*, 1804–1828. https://doi.org/10.1007/s11430-013-4679-1

Zhang, Y., Yao, H., Yang, H.-Y., Cai, H. T., Fang, H., Xu, J., et al. (2018). 3-D crustal shear-wave velocity structure of the Taiwan Strait and Fujian, SE China, revealed by ambient noise tomography. *Journal of Geophysical Research*, *123*, 8016–8031. https://doi.org/10.1029/2018jb015938

Zhang, Z., Yao, H., & Yang, Y. (2020). Shear wave velocity structure of the crust and upper mantle in Southeastern Tibet and its geodynamic implications. *Science China Earth Sciences*, *63*, 1278–1293. https://doi.org/10.1007/s11430-020-9625-3

Zhao, Y., Ye, G., Dong, J., Wei, W. B., & Jin, S. (2019). Electrical constraints on the channel flow underneath the northeastern Tibetan plateau: Results of the Longriba-Minjiang magnetotelluric sounding profile. *Journal of Asian Earth Sciences*, *170*, 73–83. https://doi.org/10.1016/j.jseaes.2018.10.004

Zheng, T., Ding, Z., Ning, J., Chang, L., Wang, X., Kong, F., et al. (2018). Crustal azimuthal anisotropy beneath the southeastern Tibetan Plateau and its geodynamic implications. *Journal of Geophysical Research: Solid Earth*, *123*, 9733–9749. https://doi.org/10.1029/2018jb015995

Zheng, X., Yao, Z., Liang, J., & Zheng, J. (2010). The role played and opportunities provided by IGP DMC of China national seismic network in Wenchuan earthquake disaster relief and researches. *Bulletin of the Seismological Society of America*, *100*, 2866–2872. https://doi.org/10.1785/0120090257

Zheng, Y., Ma, H., Lu, J., Ni, S., Li, Y., & Wei, S. (2009). Source mechanism of strong aftershocks (M s≥5.6) of the 2008/05/12 Wenchuan earthquake and the implication for seismotectonics. *Science in China - Series D: Earth Sciences*, *52*, 739–753. https://doi.org/10.1007/s11430-009-0074-3